Analytic expressions for the angular and the spectral fluxes at Compton X-ray sources

M. Jacquet* and C. Bruni

Laboratoire de l'Accélérateur Linéaire, Orsay, France. *Correspondence e-mail: mjacquet@lal.in2p3.fr

The goal of this paper is to express simply the number of photons impinging on a target in the framework of accelerator-based Compton X-ray sources. From the basic kinematics of Compton sources, analytic formulas for the angular and the spectral fluxes are established as functions of the energy spread or/and the angular divergence of the electron and the laser beams. Their detailed predictions are compared with Monte Carlo simulations. These analytic expressions allow one to compute in a simple and precise way the X-ray flux in a given angular acceptance and a given energy bandwidth, knowing the characteristics of the incoming beams.

1. Introduction

Today, Compton X-ray sources are in full development thanks to the exceptional improvement of high-power lasers over the last 15 years. The principle is based on the production of X-ray pulses of a few tens of keV in energy by Compton back-scattering of intense laser light of micrometric wavelength against an electron bunch of tens of MeV in energy (*i.e.* about 100 times less energetic than electrons used to produce synchrotron radiation in the X-ray range). Such Compton sources are compact installations (with areas of $\sim 100 \, \mathrm{m}^2$) which provide high-intensity, high-quality X-ray beams with a tunable energy. The present most ambitious projects aim at producing a total flux of 10^{12}–10^{14} photons s^{-1} (Jacquet, 2014) that gives access to experimental methods currently used at synchrotron beamlines. For various applications, the development of these sources will allow the use of powerful analysis techniques in such environments as hospitals, laboratories or museums. The diversity of the possible applications of these sources increases the demand for a simple formulation of the X-ray flux available at a target sample with an intuitive understanding of its spectral and spatial properties. Our motivation is to guide the users when evaluating the performances of such sources in their domain of competence (medical, materials, art history, *etc.*). Indeed, to our knowledge, there is no analytic formulas in the literature describing angular and spectral X-ray fluxes expected from a given Compton source. There are some analogies between synchrotron radiation sources and Compton sources, but the spectral and the spatial properties are different. Thus, Compton backscattering sources need a specific description. Our analytic formulas provide the flux within a finite polar angle around the electron beam direction and within a finite bandwidth around the Compton edge. The energy spread and the angular divergence of the electron beam and of the laser affect the X-ray flux in the chosen kinematic region. The estimation of such effects is the purpose of this article. The
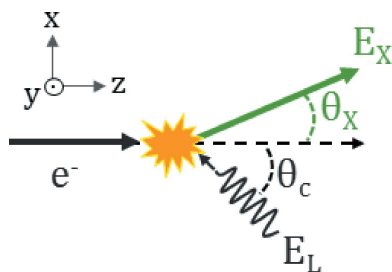
analytic expressions are obtained by convolving purely kinematic effects with expressions that characterize the laser and the electron beam properties.

The basic principles of a Compton source, the kinematics and our calculation framework are described in §2. The performances of current laser systems are such that the main impact on the Compton source characteristics comes from the angular divergence σ_e' and the energy spread σ_e of the incident electron beam. The latter may vary widely depending on the chosen accelerator complex (see §2.2). Analytic expressions for the total X-ray flux and for its angular and spectral dependences are established in §3 and §4 as functions of these two electron beam parameters and compared with Monte Carlo simulations.

2. Key parameters for the X-ray flux

This section introduces the key parameters needed to understand the analytic developments that follow.

2.1. The Compton process

Fig. 1 describes the Compton scattering between a free relativistic electron of Lorentz factor γ and a photon of energy E_L which is the basic process exploited in an accelerator-based X-ray source.

Electrons of a few tens of MeV are used in X-ray sources whereas the laser is usually in the infrared domain. In the laboratory frame, the scattered photon energy E_X varies quadratically with the electron energy and linearly with the laser photon energy E_L. Assuming $\gamma \gg 1$ and the laser photon energy is small compared with the electron rest mass energy, we can derive from the kinematics of the process

$$E_X = \frac{E_m}{1 + \gamma^2 \theta_X^2}, \tag{1a}$$

$$E_m = 2\gamma^2 E_L (1 + \cos \theta_c), \tag{1b}$$

where θ_c is the collision angle and θ_X the scattering polar angle of the Compton photon with respect to the incoming electron momentum. Equation (1a) implies an univocal dependence between the energy of the backscattered photon and its emission angle θ_X. Photons of maximum energy E_m are those emitted on-axis ($\theta_X = 0°$). For an X-ray which is produced by an electron of Lorentz factor γ, let ε be the ratio of E_X and E_m.
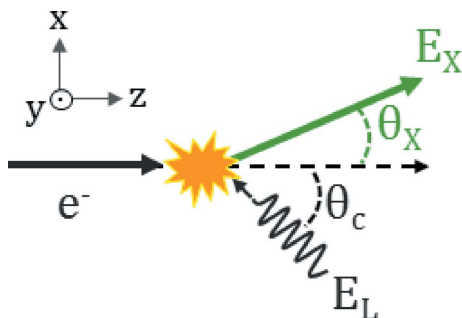
Figure 1
Schematic drawing of the scattering process between an electron and a laser photon. xyz is the laboratory frame.

The dependence on ε of the normalized differential cross section p_{E_X} can be expressed as (Telnov, 2000)

$$p_{E_X}(\varepsilon) = \frac{dp}{d\varepsilon} = \frac{3}{2}(1 - 2\varepsilon + 2\varepsilon^2), \tag{2a}$$

$$\varepsilon \equiv E_X / E_m. \tag{2b}$$

Equations (1a), (1b), (2a) and (2b) will be the key relations used to establish the analytic expressions for the X-ray flux in a given spectral bandwidth or/and within a given angular acceptance, and to quantify the reduction of the angular and spectral fluxes due to the energy spread and the angular divergence of the two colliding beams.

The Compton X-ray sources involve multi-collisions between a laser pulse and an electron bunch. Thus, to establish the total X-ray flux, we need to take into account the laser pulse and the electron bunch sizes. Let n_e and n_L be, respectively, the number of electrons per bunch and the number of photons per laser pulse, and let $x_{e,L}$, $y_{e,L}$ and $z_{e,L}$ be the transverse and longitudinal dimensions (r.m.s.) of the electron bunch and laser pulse at the interaction point. Assuming the electron beam and the laser have Gaussian distributions in the three dimensions, for electron–photon collisions taking place with a crossing angle θ_c in the xz plane, the number of X-ray produced per second is (Suzuki, 1976)

$$F(\theta_c) = \frac{\Sigma_{th}\, n_e n_L f_{rep}}{2\pi \left[(x_e^2 + x_L^2) + \tan^2(\theta_c/2)(z_e^2 + z_L^2)\right]^{1/2} \left(y_e^2 + y_L^2\right)^{1/2}}. \tag{3}$$

$F(\theta_c)$ is proportional to the Thomson cross section Σ_{th}, the luminosity and the repetition frequency of the interactions f_{rep}. High X-ray fluxes are foreseen in various projects. For example, ThomX (Variola *et al.*, 2014)) foresees $F(0) \simeq 10^{13}$ photons s^{-1} with $E_m = 45$ keV for a 50 MeV electron bunch ($\gamma = 100$) of 1 nC, micrometric wavelength laser pulses of 10 mJ, $f_{rep} = 20$ MHz, and $x_{e,L}, y_{e,L} \simeq 40$ μm.

Expression (3) will be our reference flux hereafter referred to as $F_0 \equiv F(\theta_c)$.

2.2. X-ray spectral bandwidth

Relations (1a) and (1b) imply that the X-ray energy spectrum produced by electrons and photons whose energies are single-valued is strictly monochromatic at a given emission angle. But the energy dispersion and the angular divergence of the stored electrons and, to a lesser extent, of the photons at the interaction point lead to a significant broadening of E_X at a given scattering angle θ_X.

The relative energy spreads (r.m.s.) of an electron bunch and of a laser pulse will be denoted by σ_e and σ_L, while their angular divergences (r.m.s.) will be denoted by σ_e' and σ_L' (assuming that the horizontal and the vertical divergences are equal). The order of magnitude of the broadening $\Delta E_X / E_X$ of the on-axis Compton spectrum due to each one of these four parameters can be estimated from equations (1a) and (1b) by replacing γ, E_L, θ_X^2 and θ_c with $\gamma(1 + \sigma_e)$, $E_L(1 + \sigma_L)$, $\sigma_e'^2$ and $\theta_c + \sigma_L'$, respectively, and performing four Taylor series

expansions of equation (1a) in σ_e, σ_L, $\sigma_e'^2$ and σ_L', resulting in: $\Delta E_X/E_X \approx 2\sigma_e$, $\Delta E_X/E_X \approx \sigma_L$, $\Delta E_X/E_X \approx \gamma^2 \sigma_e'^2$ and $\Delta E_X/E_X \approx (\cos\theta_c\, \sigma_L'^2/2 + \sin\theta_c\, \sigma_L')/(1+\cos\theta_c)$ due to σ_e, σ_L, σ_e' and σ_L', respectively.

We will give now orders of magnitude for these σ_e, σ_L, σ_e' and σ_L' parameters for current electron guns and pulsed lasers:

(i) The normalized horizontal and vertical emittances $\gamma x_e \sigma_e'$ and $\gamma y_e \sigma_e'$ of ~ 1 nC bunches delivered by good quality current electron guns are 1–5 mm mrad (Arnold & Teichert, 2011; Rao & Dowell, 2013). With these values, transverse sizes and normalized divergences are typically x_e, $y_e \simeq 20$–100 µm and $\gamma\sigma_e' \simeq 0.01$–$0.25$ rad, respectively.

(ii) Concerning σ_e, the electron beam relative energy spread, current values at electron accelerators are of a few 10^{-3} up to a few percent.

(iii) On the laser side, the product of ΔE_L, the r.m.s. energy bandwidth of the pulse, and Δt_L, its r.m.s. temporal duration, is constrained by the uncertainty principle (Donnelly & Grossman, 1998) $\Delta E_L \Delta t_L \geq \hbar/2$. Unchirped pulses have the minimum time-bandwidth product, i.e. close to $\hbar/2$, whereas larger values prevail for chirped pulses. Then, let us consider a laser with a wavelength λ, and an r.m.s. pulse duration Δt_L. Assuming unchirped pulses, one derives from the uncertainty principle: $\sigma_L \equiv \Delta E_L/E_L = \lambda/(4\pi c \Delta t_L)$, where c is the speed of light. It follows that infrared fs–ps pulses have a relative energy spread σ_L of a few 10^{-5} (for 10 ps pulses) up to a few 10^{-3} (for 100 fs pulses).

(iv) In good quality lasers with Gaussian pulses, the relation between the r.m.s. transverse pulse sizes x_L, y_L and the angular divergence σ_L' is $x_L\sigma_L' = y_L\sigma_L' = \lambda/(4\pi)$ (Schmüser et al., 2008), leading to the following typical values: x_L, $y_L \simeq 10$–100 µm and $\sigma_L' \simeq 1$–10 mrad (infrared laser).

Table 1 summarizes these orders of magnitude and the corresponding broadening of the Compton spectrum $\Delta E_X/E_X$. The spectrum broadening due to the laser bandwidth σ_L is negligible, as well as the broadening due to the laser divergence if the product $\sin\theta_c\sigma_L'$ is smaller than ~ 1 mrad, which is the case in almost all current Compton projects where electrons and laser photons collide head-on (Jacquet, 2014). We conclude that $\Delta E_X/E_X$ is mainly governed by the angular divergence and the relative energy spread of the electron beam.

2.3. Input and notations

In this section, we introduce the probability distributions used to establish the analytic expressions of §3 and §4. The nominal Lorentz factor of the electron beam will be referred to as γ_0. Then the Lorentz factor of a given electron is written as $\gamma = (1+\delta\gamma)\gamma_0$, where $\delta\gamma$ is the difference in energy of this electron with respect to the nominal beam energy (E_0) divided by E_0. With θ_c being the nominal value of the crossing angle between the electron beam and the laser in the xz plane (see Fig. 1), we define ζ_{ex}, ζ_{ey}, $\theta_c + \zeta_{Lx}$ and ζ_{Ly} as the angles to z axis of the projections of the momentum of a given electron and of a given laser photon in the xz and yz planes. The probability distributions of $\delta\gamma$, $\zeta_{ex,ey}$ and $\zeta_{Lx,Ly}$ are assumed to be Gaussian

Table 1
Orders of magnitude of the relative energy spread and divergence of electron and laser beams at the interaction point, and associated broadening of the Compton spectrum.

Variable	Typical values	$\Delta E_X/E_X$
σ_e	10^{-3}–10^{-2}	2×10^{-3}–2×10^{-2}
σ_L	10^{-5}–10^{-3}	10^{-5}–10^{-3}
$\gamma\sigma_e'$ (rad)	0.01–0.25	10^{-4}–10^{-1}
σ_L' (mrad)	1–10	10^{-7}–10^{-3} ($\sin\theta_c\sigma_L' \lesssim 1$ mrad)
		10^{-3}–10^{-2} ($\sin\theta_c\sigma_L' \simeq 1$–$10$ mrad)

with standard deviations σ_e, $\sigma_{ex,ey}'$ and $\sigma_{Lx,Ly}'$, respectively. We further assume $\sigma_{ex}' = \sigma_{ey}' = \sigma_e'$ and $\sigma_{Lx}' = \sigma_{Ly}' = \sigma_L'$. ζ_{eLx} (ζ_{eLy}, respectively) is defined as the convolution of the ζ_{ex} and ζ_{Lx} distributions (of ζ_{ey} and ζ_{Ly}, respectively) and follows a Gaussian distribution whose standard deviation is $\sigma_{eL}' = (\sigma_e'^2 + \sigma_L'^2)^{1/2}$.

We introduce also the polar and azimuthal angles with respect to the z-axis direction (see Fig. 2), ζ_e and φ_e, of an electron momentum ($\zeta_{ex} = \zeta_e\cos\varphi_e$, $\zeta_{ey} = \zeta_e\sin\varphi_e$, $\zeta_e^2 = \zeta_{ex}^2 + \zeta_{ey}^2$), and similarly ζ_X and φ_X for a photon scattered by this electron. For small ζ_e and ζ_X (i.e. when $\sin\zeta_e \simeq \zeta_e$ and $\sin\zeta_X \simeq \zeta_X$), the polar angle θ_X of the backscattered photon with respect to the electron momentum is $\theta_X^2 = \zeta_e^2 + \zeta_X^2 - 2\zeta_e\zeta_X\cos(\varphi_e - \varphi_X)$. Summing over azimuthal angles we obtain

$$\theta_X^2 = \zeta_e^2 + \zeta_X^2. \tag{4}$$

The θ_X angle averaged over φ_e and φ_X expressed in (4) is the one that appears in equation (1a).

Explicitly, the probability distributions of $\delta\gamma$, $\zeta_{eLx,eLy}$ and ζ_e^2 defined in the ranges $]-\infty, +\infty[$, $]-\infty, +\infty[$ and $[0 + \infty[$, respectively, are

$$\frac{dp}{d(\delta\gamma)} = \frac{1}{\sqrt{2\pi}\sigma_e}\exp[-(\delta\gamma)^2/2\sigma_e^2], \tag{5a}$$

$$\frac{dp}{d\zeta_{eLx,eLy}} = \frac{1}{\sqrt{2\pi}\sigma_{eL}'}\exp[-(\zeta_{eLx,eLy})^2/2\sigma_{eL}'^2], \tag{5b}$$

$$\frac{dp}{d(\zeta_e^2)} = \frac{1}{2\sigma_e'^2}\exp(-\zeta_e^2/2\sigma_e'^2). \tag{5c}$$

In the following sections we will obtain analytic expressions for the ratios $R_{tot} = F_{tot}/F_0$, $R_\alpha = F_\alpha/F_0$, $R_{bw} = F_{bw}/F_0$ and $R_{\alpha,bw} = F_{\alpha,bw}/F_0$, where F_{tot} is the total flux, F_α the flux in a given angular acceptance α (of a few milliradians) around the
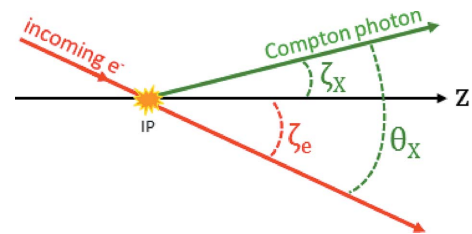
Figure 2
Polar angles of an electron momentum (ζ_e) and of a Compton photon (ζ_X) scattered by this electron with respect to the z-axis, and polar angle θ_X of the Compton photon with respect to the electron momentum. Note that the electron momentum is practically not affected by the collision.

z-axis direction, F_{bw} the flux in a given energy bandwidth (bw) centered at the on-axis X-ray energy $E_m^0 = 2\gamma_0^2 E_L(1 + \cos\theta_c)$, and $F_{\alpha,bw}$ the flux in a given angular acceptance and a given energy bandwidth. We will study the dependence of these ratios on the σ_e' and σ_e parameters which govern the broadening of the Compton angular spectrum as discussed in §2.2, and we will confront our formulas with simulations performed with the *CAIN* code (Yokoya, 2003) generated with several σ_e' and σ_e values, all other parameters (n_e, n_L, f_{rep} x_e, y_e, x_L, y_L, z_e and z_L) remaining fixed. In the *CAIN* simulations, we use $\gamma_0 = 100$ (*i.e.* the order of magnitude to produce Compton backscattered photons in the X-ray domain), a laser wavelength $\lambda = 1\,\mu m$, and we assume a pulse waist of 40 µm. For a full range coverage of the electron beam parameters in current accelerators (see Table 1), the σ_e' and σ_e ranges used for this work are $\gamma\sigma_e' \simeq 0.01$–$0.25$ rad (*i.e.* $\sigma_e' \simeq 0$–2.5 mrad for $\gamma \simeq 100$) and $\sigma_e \simeq 0$–2%.

3. Spectral or angular selection

In this section, we will obtain the expression of the X-ray flux when one selects *either* the energy *or* the emission angle of the X-rays.

3.1. Dependence of the total flux F_{tot} on the electron and the laser beam angular divergences

Since we assume here that no cut is applied to the X-ray energy, the electron beam energy spread does not come into this calculation. Thus we treat here only the electron beam and the laser beam divergences. We consider the collision of an electron with a photon at a nominal crossing angle θ_c in the horizontal plane xz. The effect of the two ζ_{eLx} and ζ_{eLy} variables (defined in §2.3) can be treated as an additional contribution to θ_c. Indeed, for small ζ_{eLx} and ζ_{eLy} (*i.e.* when $\sin\zeta_{eLx} \simeq \zeta_{eLx}$ and $\sin\zeta_{eLy} \simeq \zeta_{eLy}$) and by making the approximation that ζ_{eLx} and ζ_{eLy} are awarded only to the electron (see Fig. 3), a geometrical calculation leads to an effective electron–photon crossing angle Θ_c such that $\Theta_c = \mathrm{acos}\{\zeta_{eLx}\sin\theta_c + \cos\theta_c[1 - (\zeta_{eLx}^2 + \zeta_{eLy}^2)]^{1/2}\}$.
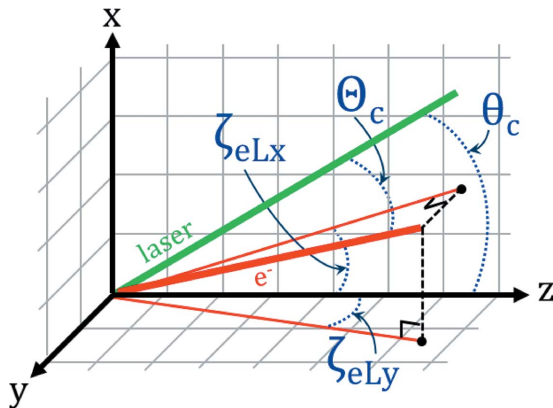
Figure 3
Nominal (θ_c) and effective (Θ_c) electron–photon crossing angles assuming that ζ_{eLx} and ζ_{eLy} are awarded only to the electron.

Then, for an electron bunch and a laser pulse of r.m.s. angular divergence σ_e' and σ_L', respectively, the total flux $F_{tot} \equiv F(\theta_c)$ is obtained by integrating $F(\Theta_c)$, weighted by the Gaussian probabilities of ζ_{eLx} and ζ_{eLy} [see equation (5b)]. Keeping up to the second-order terms in ζ_{eLx} and ζ_{eLy} results in the following expression for the ratio $R_{tot} \equiv F_{tot}/F_0$:

$$R_{tot} = 1 - \frac{[1 + \tan^2(\theta_c/2)]^2\,[1 - \frac{1}{2}r_{xz}\tan^2(\theta_c/2)]}{4[1 + r_{xz}\tan^2(\theta_c/2)]^2}$$
$$\times\, r_{xz}(\sigma_e'^2 + \sigma_L'^2), \tag{6}$$

where $r_{xz} = (z_e^2 + z_L^2)/(x_e^2 + x_L^2)$. For $x_e = 72\,\mu m$, $x_L = 40\,\mu m$, $z_e = 4.8$ mm, $z_L = 3$ mm and $\sigma_L' = 2$ mrad (*i.e.* the laser beam divergence value corresponding to a 40 µm waist size), R_{tot} is shown in Fig. 4 as a function of σ_e', for $\theta_c = 0°$, $1°$ and $2°$, and compared with results obtained with the *CAIN* simulation program. The analytic expression reproduces well the differences between the various collision angle cases. A reduced collision angle amplifies the divergence impact on the total flux but only to a small extent, less than 1% for head-on collisions.

3.2. X-ray flux in a given energy bandwidth (F_{bw})

In this section we look at the number of X-rays produced when an energy cut is applied. For this, the electron energy spread is decisive whereas F_{bw}/F_{tot} is independent of the electron beam angular divergence since no angular selection is assumed here. Also, we do not take into account the broadening of the Compton spectrum ($\Delta E_X/E_X \simeq 10^{-3}$–$10^{-2}$) that occurs in the particular case where both the laser divergence and the collision angle are large (see Table 1).

Let us consider an electron of Lorentz factor $\gamma = \gamma_0(1 + \delta\gamma)$. The energy of a photon which is backscattered by this electron is E_X and, according to equation (1b), the maximum value of E_X is $E_m = E_m^0(1 + \delta\gamma)^2$ where $E_m^0 = 2\gamma_0^2 E_L(1 + \cos\theta_c)$. The
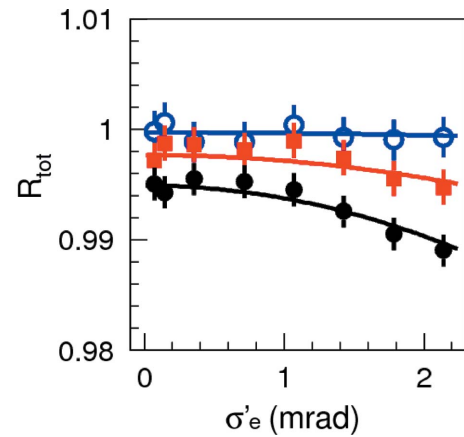
Figure 4
The ratio $R_{tot} = F_{tot}/F_0$ as a function of σ_e' for a laser divergence $\sigma_L' = 2$ mrad, for $\theta_c = 0°$ (black bullets, black line), $1°$ (red squares, red line) and $2°$ (blue open circle, blue line). Points are *CAIN* simulations. For each point, the error bar indicates the statistical uncertainty calculated from the number of generated events (namely $\sim 4.7 \times 10^5$, 4.1×10^5 and 3.1×10^5 events for each of the eight points generated with $\theta_c = 0°$, $1°$ and $2°$, respectively). Lines illustrate the analytic formula [equation (6)] results.

ratio E_X/E_m^0 is denoted by ε_0. F_{bw} is the flux of photons whose ε_0 lies in the interval between $1 - bw$ and $1 + bw$. The energy probability distribution (2a) expressed as a function of ε_0 becomes

$$p_{E_X}(\varepsilon_0) = \frac{3}{2}\left[1 - \frac{2\varepsilon_0}{(1+\delta\gamma)^2} + \frac{2\varepsilon_0^2}{(1+\delta\gamma)^4}\right]\frac{1}{(1+\delta\gamma)^2}. \quad (7)$$

Fig. 5 shows this distribution for three different cases: $\delta\gamma < 0$, $\delta\gamma = 0$ and $\delta\gamma > 0$. Since p_{E_X} is a quasi-linear function for ε_0 larger than ~ 0.65, the integral of p_{E_X} between ε_{0_1} and ε_{0_2} can be approximated by $p_{E_X}[(\varepsilon_{0_1} + \varepsilon_{0_2})/2](\varepsilon_{0_2} - \varepsilon_{0_1})$. Thus F_{bw} is calculated in the following way (see Fig. 5):

(i) Electrons with $\delta\gamma$ such that $(1+\delta\gamma)^2 < 1 - bw$ do not contribute to F_{bw}.

(ii) The contribution to F_{bw} of electrons having a relative energy difference $\delta\gamma$ such that $1 - bw < (1+\delta\gamma)^2 < 1 + bw$ is denoted by $f_{bw}^s(\delta\gamma)$ and is equal to the integral of p_{E_X} between $\varepsilon_{0_1} = 1 - bw$ and $\varepsilon_{0_2} = (1+\delta\gamma)^2$ (green area): $f_{bw}^s(\delta\gamma) = p_{E_X}\{[(1 - bw) + (1+\delta\gamma)^2]/2\}[(1+\delta\gamma)^2 - (1 - bw)]$. These electrons are denoted by $\delta\gamma_s$ in Fig. 5.

(iii) The contribution of electrons whose $\delta\gamma$ satisfies $1 + bw < (1+\delta\gamma)^2$ is denoted by $f_{bw}^L(\delta\gamma)$ and is equal to the integral of p_{E_X} between $\varepsilon_{0_1} = 1 - bw$ and $\varepsilon_{0_2} = 1 + bw$ (area hatched in green): $f_{bw}^L(\delta\gamma) = p_{E_X}(1)\,2bw$. These electrons are denoted by $\delta\gamma_L$ in Fig. 5.

Assuming that the $\delta\gamma$ variable follows the Gaussian distribution (5a) where $\sigma_e \simeq 0$–2%, one can make the approximation $(1+\delta\gamma)^2 \simeq 1 + 2\delta\gamma$ and R_{bw} can be written

$$R_{bw} = R_{tot}\left[\int_{-bw/2}^{bw/2}\frac{1}{\sqrt{2\pi}\sigma_e}\exp\left(-\delta\gamma^2/2\sigma_e^2\right)f_{bw}^s(\delta\gamma)\,\mathrm{d}(\delta\gamma)\right.$$
$$\left. + \int_{bw/2}^{+\infty}\frac{1}{\sqrt{2\pi}\sigma_e}\exp\left(-\delta\gamma^2/2\sigma_e^2\right)f_{bw}^L(\delta\gamma)\,\mathrm{d}(\delta\gamma)\right].$$

Performing a first-order Taylor expansion in $\delta\gamma$, the calculation of the above integrals leads to
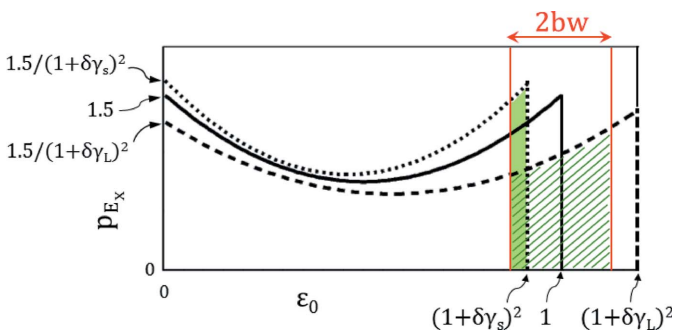
Figure 5
Differential cross section p_{E_X} for three electron populations: electrons with positive $\delta\gamma$ (dotted line), with $\delta\gamma = 0$ (solid line), and with negative $\delta\gamma$ (dashed line), as a function of the scattered photon energy $\varepsilon_0 = E_X/E_m^0$. Also represented are f_{bw}^s (green area) and f_{bw}^L (area hatched in green).
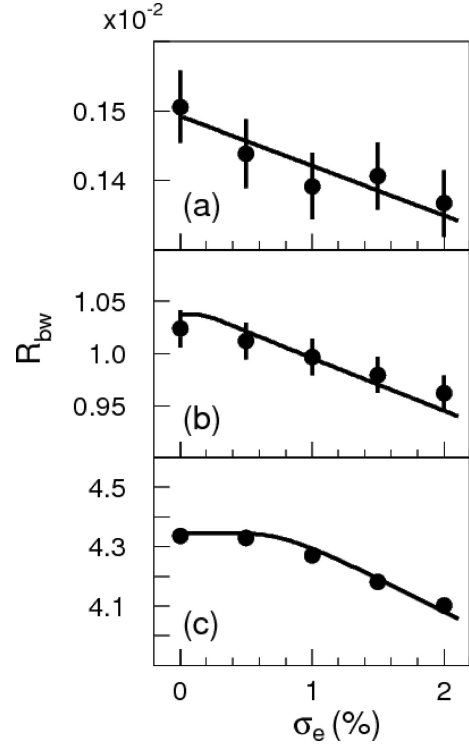
Figure 6
The ratio $R_{bw} = F_{bw}/F_0$ as a function of σ_e for three energy bandwidths: (a) bw = 0.1%, (b) bw = 0.7% and (c) bw = 3%. Points are *CAIN* simulations and the error bars indicate the statistical uncertainties. Lines are obtained using the analytic formula (8).

$$R_{bw} = \frac{3}{2}R_{tot}\,bw\left\{1 - \left(bw - bw^2/2\right)\mathrm{ERF}\left[bw/(2\sqrt{2}\sigma_e)\right]\right.$$
$$\left. - 6\sqrt{2/\pi}\,\sigma_e\exp\left(-bw^2/8\sigma_e\right)\right\}, \quad (8)$$

and is shown in Fig. 6 as a function of σ_e, for three energy bandwidths: (a) bw = 0.1%, (b) bw = 0.7% and (c) bw = 3%.

First of all, in the absence of any energy spread, one notes a factor 3/2 compared with the classical formula used for synchrotron radiation, showing the need for a proper analytic development when dealing with Compton sources. This factor, which comes from the Compton cross section, remains whatever the selected energy acceptance. Fig. 6 shows that a linear behavior of the flux reduction with σ_e prevails if the selected bandwidth is small compared with σ_e (as in the 0.1% and 0.7% cases and in the right-hand region of the 3% case), whereas the flux remains globally constant when the energy acceptance is large with respect to σ_e (as in the left-hand region of the 3% case). In the three bandwidth cases, the small systematic difference between the *CAIN* simulation values and the analytic results for $\sigma_e \simeq 2\%$ shows that higher-order terms in $\delta\gamma$ have to be taken into account for σ_e values larger than 2–3%. In any event, the reduction due to the energy spread is less than 10% in the parameter range considered here.[1]

---

[1] In the particular case of a Compton machine design such that $\sin\theta_e\sigma_L' \simeq$ 1–10 mrad, the effect of the laser divergence leads to a reduction of R_{bw} from a few per million to a few percent depending on θ_e, σ_L' and bw. The largest effect occurs for $\theta_e = 90°$ and $\sigma_L' \simeq 10$ mrad and would result for instance in a decrease of $R_{0.1\%}$ and $R_{3\%}$ by about 5% and 1%, respectively.

3.3. X-ray flux in a given angular acceptance

We now consider the photon flux F_α within a given angular acceptance α. In this case, the effect of an energy spread is completely negligible since the mean value of $\delta\gamma$ vanishes.

For any value of the polar angle θ, the $\gamma_0^2\theta^2$ product is denoted as μ_θ. Let us consider an electron whose momentum makes a polar angle ζ_e with respect to the z axis (see Fig. 2) while the photon backscattered by this electron has a polar angle ζ_X. Using equations (1a), (2a) and (4), the dependence of the normalized differential Compton cross section on μ_{ζ_X} is given by

$$p_\mu(\mu_{\zeta_X}) = \frac{d}{d\mu_{\zeta_X}} = \frac{3}{2}\frac{1 + (\mu_{\zeta_X} + \mu_{\zeta_e})^2}{(1 + \mu_{\zeta_X} + \mu_{\zeta_e})^4}. \quad (9)$$

This distribution is shown in Fig. 7 for $\mu_{\zeta_e} = 0$ and $\mu_{\zeta_e} = 0.04$. Here again, with p_μ being a quasi-linear function of μ_{ζ_X} for μ_{ζ_X} smaller than ~ 0.15, its integral between $\mu_{\zeta_{X_1}}$ and $\mu_{\zeta_{X_2}}$ can be approximated by $p_\mu\{[\mu_{\zeta_{X_1}} + \mu_{\zeta_{X_2}}]/2\}(\mu_{\zeta_{X_1}} - \mu_{\zeta_{X_2}})$. Then, as illustrated by Fig. 7, an electron contribution to F_α is equal to $\mu_\alpha p_\mu(\mu_\alpha/2)$ and, according to the exponential distribution (5c) of ζ_e^2, the ratio R_α for an electron bunch of r.m.s. divergence $\sigma'_{ex} = \sigma'_{ey} = \sigma'_e$ can be simply expressed as

$$R_\alpha = R_{tot}\,\mu_\alpha \int\limits_0^{+\infty} \frac{1}{2\sigma_e'^2}\exp(-\zeta_e^2/2\sigma_e'^2)\,p_\mu(\mu_\alpha/2)\,d(\zeta_e^2). \quad (10)$$

The calculation of equation (10) using a first-order Taylor series expansion in ζ_e^2 leads to

$$R_\alpha = \frac{3}{2}R_{tot}\frac{\mu_\alpha}{(1 + \mu_\alpha/2)^2}$$
$$\times \left[1 + \frac{\mu_\alpha^2}{4} - 4\gamma_0^2\sigma_e'^2\frac{2 - \mu_\alpha/2 + \mu_\alpha^2/4}{1 + \mu_\alpha/2}\right]. \quad (11)$$

Expression (11) is valid as long as μ_α and $\gamma_0^2\sigma_e'^2$ are less than ~ 0.15 and ~ 0.03, respectively. For larger values of μ_α, the linear approximation of p_μ is no longer valid and the integral between 0 and μ_α must be explicitly calculated. For $\gamma_0^2\sigma_e'^2 \gtrsim 0.03$, higher-order terms in ζ_e^2 have to be taken into account in the series expansion of equation (10). R_α and points obtained with *CAIN* are shown in Fig. 8 as a function of σ'_e (for $\gamma_0 = 100$) for an anglular acceptance α of 1 mrad and 2 mrad. Equation (11) is represented by the solid lines and is in very good
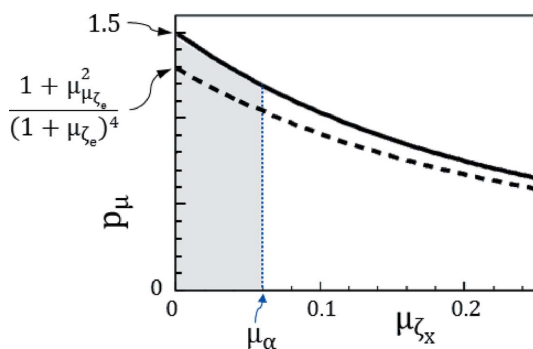
Figure 7
The angular differential cross section p_μ as a function of μ_{ζ_X} for $\mu_{\zeta_e} = 0$ (solid line) and for $\mu_{\zeta_e} = 0.04$ (dashed line). The shaded area shows the contribution to F_α of an electron whose momentum has a polar angle ζ_e.
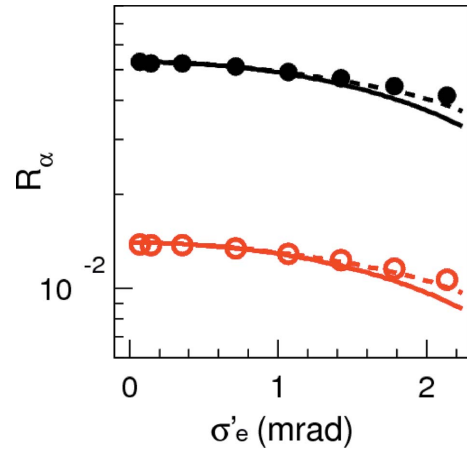
Figure 8
The ratio $R_\alpha = F_\alpha/F_0$ as a function of σ'_e for an angular acceptance α of 1 mrad (open red circles and red line) and 2 mrad (black bullets and black line). Points are *CAIN* simulations (the error bars are too small to be visible). Solid lines are obtained with equation (11), dotted lines show R_α calculated to third order in ζ_e^2.

agreement with *CAIN* simulations up to $\sigma'_e \simeq 1.5$ mrad. The need to take into account higher-order terms in ζ_e^2 in the modeling of R_α for large values of σ'_e is highlighted for $\sigma'_e \simeq 2$ mrad. The dotted lines indicate the analytic expression results when the third-order term in ζ_e^2 is taken into account.[2]

4. X-ray flux within a given angular acceptance and a given energy bandwidth

In this section we assume that both an angular cut and an energy selection are applied to the backscattered photons and we calculate the consequent reduction of the X-ray flux. In the first two subsections, the electron beam divergence and its energy spread will be treated independently to understand the impact of each one of these parameters. Then we will take into account both of these beam characteristics.

4.1. Dependence on the electron beam angular spread

Our starting point is equation (8) which gives the X-ray yield in a given energy bandwidth, and we will modify this expression to take into account the angular acceptance defined by a maximum value α of the X-ray emission direction with respect to the z axis and the electron beam angular spread. In order to achieve a single formulation, we associate an angle to the energy bandwidth, namely $\theta_{bw} = \sqrt{bw}/\gamma_0$. At this stage, we have to treat separately the $\alpha < \theta_{bw}$ case and the $\alpha > \theta_{bw}$ case, as illustrated in Fig. 9. The dashed red line represents the electron momentum direction which makes an angle ζ_e with respect to the z direction. α defines the angular cut and θ_{bw} the energy acceptance translated into an angle. More precisely, to the energy bandwidth (or energy acceptance) bw corresponds an angular acceptance which is a cone whose axis is the momentum of the electron which backscatters the incoming photon and whose half aperture is θ_{bw}. In

---

[2] We do not give here the expression of this third-order analytic formula since it is relatively heavy and since equation (11) reproduces sufficiently well the simulations in our parameter range.
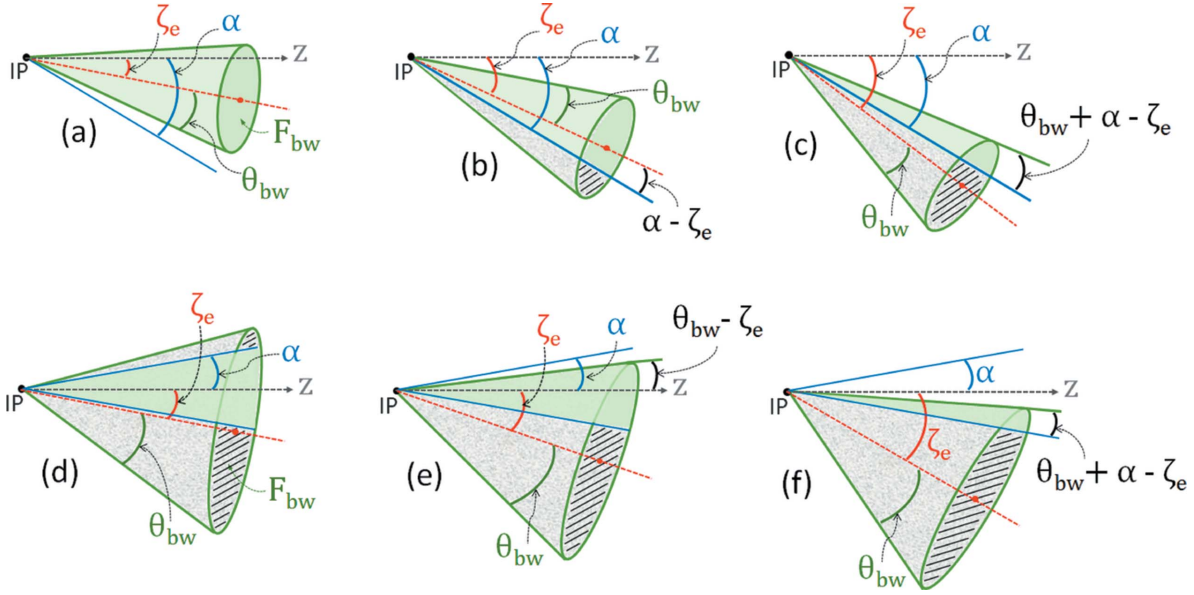
Figure 9
Top: the $\alpha > \theta_{bw}$ case where $\theta_{bw} = \sqrt{bw}/\gamma_0$. Three configurations are shown: (a) $\zeta_e < \alpha - \theta_{bw}$, (b) $\alpha - \theta_{bw} < \zeta_e < \alpha$, (c) $\alpha < \zeta_e < \alpha + \theta_{bw}$. Bottom: the $\alpha < \theta_{bw}$ case. (d) $\zeta_e < \theta_{bw} - \alpha$, (e) $\theta_{bw} - \alpha < \zeta_e < \theta_{bw}$, (f) $\theta_{bw} < \zeta_e < \alpha + \theta_{bw}$.

Fig. 9, those X-rays which pass both the angular and the energy cuts are the ones emitted in the green domain. The hatched regions show emission directions which are outside the X-ray angular acceptance cone of aperture α. The accepted region depends on the three angles involved in the following way:

(i) For $\alpha > \theta_{bw}$ (see upper panels in Fig. 9) and values of ζ_e such that $\zeta_e < \alpha - \theta_{bw}$, all the X-rays whose energy belong to the accepted bandwidth pass the angular cut [case (a)]; when ζ_e increases, the cone intersection diminishes and depends on whether ζ_e is larger than α or not [(b) and (c) cases];

(ii) For $\alpha < \theta_{bw}$ (see lower panels in Fig. 9), the cone intersection is reduced as the electron angular spread increases and depends on whether ζ_e is larger than θ_{bw} or not [(e) and (f) cases].

To take into account the various cases enumerated above, we introduce the following two angles: $\theta_m = \min(\alpha, \theta_{bw})$ and $\theta_M = \max(\alpha, \theta_{bw})$. Then, using the ζ_e^2 probability distribution of equation (5c), an integration is performed for each of the three cases and the number of X-rays backscattered in the angular acceptance α and within a given energy bandwidth bw is given by the following expression:

$$R_{\alpha,bw}(\sigma_e') = R_{bw}\left[\int_0^{(\alpha-\theta_{bw})^2} \frac{1}{2\sigma_e'^2} \exp\left(-\zeta_e^2/2\sigma_e'^2\right) \frac{\theta_m^2}{\theta_{bw}^2}\, d(\zeta_e^2)\right.$$

$$+ \int_{(\alpha-\theta_{bw})^2}^{\theta_M^2} \frac{1}{2\sigma_e'^2} \exp\left(-\zeta_e^2/2\sigma_e'^2\right) \left[\frac{\theta_m^2}{\theta_{bw}^2} - \frac{\theta_m^2 - (\theta_M - \zeta_e)^2}{2\theta_{bw}^2}\right] d(\zeta_e^2)$$

$$\left.+ \int_{\theta_M^2}^{(\alpha+\theta_{bw})^2} \frac{1}{2\sigma_e'^2} \exp\left(-\zeta_e^2/2\sigma_e'^2\right) \frac{(\theta_{bw} + \alpha - \zeta_e)^2}{2\theta_{bw}^2}\, d(\zeta_e^2)\right], \quad (12)$$

where R_{bw} is given by equation (8) with $\sigma_e \simeq 0$, i.e. $R_{bw} = (3/2)\, R_{tot}\, bw[1 - (bw - bw^2/2)]$. Equation (12) leads to the following analytic expression for $R_{\alpha,bw}$:

$$R_{\alpha,bw}(\sigma_e') = \frac{R_{bw}}{\theta_{bw}^2}\left(\theta_m^2 + \sigma_e'^2\left\{\exp\left[-(\alpha - \theta_{bw})^2/2\sigma_e'^2\right]\right.\right.$$

$$\left. - \exp\left[-(\alpha + \theta_{bw})^2/2\sigma_e'^2\right]\right\}$$

$$+ \frac{\sqrt{\pi}}{\sqrt{2}}\, \sigma_e'\, \theta_M\, \text{ERF}\left(\frac{\theta_M - \theta_m}{\sqrt{2}\sigma_e'}\right)$$

$$+ \frac{\sqrt{\pi}}{\sqrt{2}}\, \sigma_e'\, \theta_m\, \text{ERF}\left(\frac{\theta_M}{\sqrt{2}\sigma_e'}\right)$$

$$\left.- \frac{\sqrt{\pi}}{\sqrt{2}}\, \sigma_e'\, (\alpha + \theta_{bw})\, \text{ERF}\left(\frac{\alpha + \theta_{bw}}{\sqrt{2}\sigma_e'}\right)\right). \quad (13)$$

CAIN simulations and results from equation (13) are shown in Fig. 10 where $R_{\alpha,bw}$ is plotted against the angular divergence σ_e' for several values of the acceptance angle α and several values of the energy bandwidth bw.

4.2. Dependence on the electron beam energy spread

We now assume $\sigma_e' = 0$ mrad and we focus on the dependence of $R_{\alpha,bw}$ on the energy spread of the electrons. We start again with the ratio R_{bw} of the X-ray flux within a given energy bandwidth bw [see equation (8)] and F_0, the X-ray flux in the 'ideal' case where $\sigma_e = \sigma_e' = 0$ [see equation (3)]. We assume that an angular selection α is applied. Only the first-order term in $\delta\gamma$ will be kept (where $\delta\gamma$ is defined in §3.2). The quantities $2|\delta\gamma|$ and $\gamma_0^2\alpha^2$ are denoted by μ_γ and μ_α, respectively. Then, depending on the relative values of μ_α and bw, three configurations have to be distinguished: (i) bw $< \mu_\alpha < 2$bw, (ii) 2bw $< \mu_\alpha$ and (iii) $\mu_\alpha <$ bw. Case (i) is illustrated in Fig. 11. In this
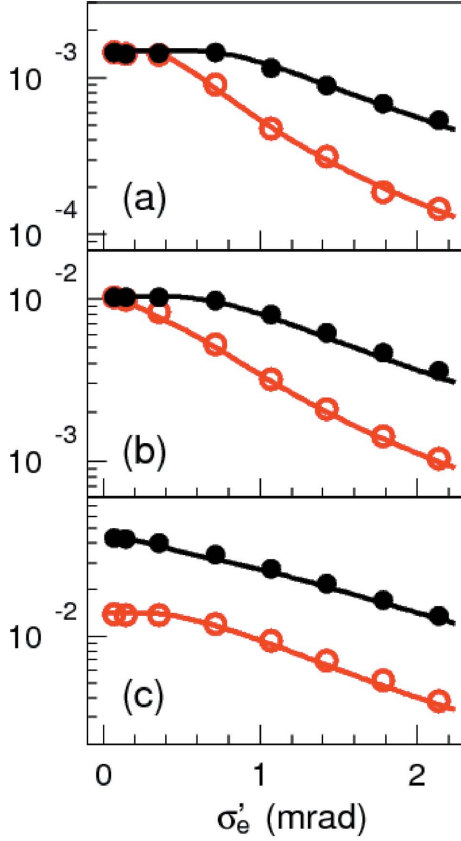
Figure 10
The ratio $R_{\alpha,\mathrm{bw}} = F_{\alpha,\mathrm{bw}}/F_0$ plotted as a function of σ'_e (assuming $\sigma_e = 0$) for $\alpha = 1$ mrad (open circles) and 2 mrad (black bullets) and for (a) bw = 0.1%, (b) bw = 0.7% and (c) bw = 3%. Lines show the results of equation (13) while points illustrate *CAIN* simulations (the error bars are too small to be visible).

figure, the energy bandwidth is assumed to be centered at $\varepsilon_0 = 1$. The left panels correspond to $\delta\gamma$ negative, the right ones to $\delta\gamma$ positive. Hatched areas represent X-rays whose energy is within the selected energy bandwidth but which are rejected by the angular cut. As shown in this figure, the size of the overlap between the energy acceptance domain and the angular acceptance one depends on bw, α and $\delta\gamma$ in the following way:

(i) For increasing values of $|\delta\gamma|$, as long as $\mu_\gamma + \mathrm{bw} < \mu_\alpha$, all X-rays accepted in the F_{bw} energy band are emitted within the angular acceptance α as shown in panels (a) and (b).

(ii) For $\mu_\alpha - \mathrm{bw} < \mu_\gamma < \mathrm{bw}$, the fraction of X-rays remaining in the μ_α angular acceptance band is $(\mathrm{bw} - \mu_\gamma + \mu_\alpha)/(2\mathrm{bw})$ [see panels (c) and (d)].

(iii) The same fraction of X-rays pass the angular cut when $\mathrm{bw} < \mu_\gamma < \mathrm{bw} + \mu_\alpha$ [panels (e) and (f)].

Similarly, the fraction of X-rays remaining in the μ_α band in the configuration (ii) defined above is 1 and $(\mathrm{bw} - \mu_\gamma + \mu_\alpha)/(2\mathrm{bw})$ for $\mu_\gamma < \mu_\alpha - \mathrm{bw}$ and $\mu_\alpha - \mathrm{bw} < \mu_\gamma < \mathrm{bw} + \mu_\alpha$, respectively. In the (iii) configuration, this fraction is μ_α/bw for $\mu_\gamma < \mathrm{bw} - \mu_\alpha$ and $(\mathrm{bw} - \mu_\gamma + \mu_\alpha)/(2\mathrm{bw})$ for $\mathrm{bw} - \mu_\alpha < \mu_\gamma < \mathrm{bw} + \mu_\alpha$.

From this and from equation (5a) which implies the following probability distribution,

$$\frac{\mathrm{d}p}{\mathrm{d}(\mu_\gamma)} = \frac{1}{\sigma_e\sqrt{2\pi}} \exp\left(-\mu_\gamma^2/8\sigma_e^2\right),$$

the following expression of $R_{\alpha,\mathrm{bw}}$ as a function of σ_e can be derived:

$$R_{\alpha,\mathrm{bw}}(\sigma_e) =$$

$$R_{\mathrm{bw}}\left[\int_0^{|\mu_\alpha - \mathrm{bw}|} \frac{1}{\sigma_e\sqrt{2\pi}} \exp\left(-\mu_\gamma^2/8\sigma_e^2\right) \frac{\min(\mu_\alpha, \mathrm{bw})}{\mathrm{bw}} \, \mathrm{d}(\mu_\gamma)\right.$$

$$\left.+ \int_{|\mu_\alpha - \mathrm{bw}|}^{\mu_\alpha + \mathrm{bw}} \frac{1}{\sigma_e\sqrt{2\pi}} \exp\left(-\mu_\gamma^2/8\sigma_e^2\right) \frac{\mu_\alpha + \mathrm{bw} - \mu_\gamma}{2\mathrm{bw}} \, \mathrm{d}(\mu_\gamma)\right], \quad (14)$$

where R_{bw} is given by equation (8). In the calculation of equation (14), a simplification occurs which makes the dependence on $\min(\mu_\alpha, \mathrm{bw})$ disappear, resulting in

$$R_{\alpha,\mathrm{bw}}(\sigma_e) = \frac{R_{\mathrm{bw}}}{2\mathrm{bw}}\left(\frac{2\sqrt{2}\sigma_e}{\sqrt{\pi}}\left\{\exp\left[-\frac{(\mu_\alpha + \mathrm{bw})^2}{8\sigma_e^2}\right]\right.\right.$$

$$\left.- \exp\left[-\frac{(\mu_\alpha - \mathrm{bw})^2}{8\sigma_e^2}\right]\right\}$$

$$+ (\mu_\alpha + \mathrm{bw})\,\mathrm{ERF}\left(\frac{\mu_\alpha + \mathrm{bw}}{2\sqrt{2}\sigma_e}\right)$$

$$\left.- (\mu_\alpha - \mathrm{bw})\,\mathrm{ERF}\left(\frac{\mu_\alpha - \mathrm{bw}}{2\sqrt{2}\sigma_e}\right)\right). \quad (15)$$

CAIN simulations and results from equation (15) are displayed in Fig. 12 where $R_{\alpha,\mathrm{bw}}$ is plotted as a function of σ_e for several values of the angular and the energy acceptances.

4.3. Combined effect of the energy spread and the angular divergence of the electron beam

When both σ_e and σ'_e must be taken into account to calculate the ratio $R_{\alpha,\mathrm{bw}}(\sigma_e, \sigma'_e)$, this analytic formulation encounters a severe limitation for the following reason. When the incoming photons are backscattered by electrons whose energies are distributed according to equation (5a), one may try to compute the X-ray flux in a way similar to that carried out in §4.1. The bw term which comes in the θ_{bw} definition would have to be replaced by $\mathrm{bw}_{\mathrm{effective}} = \mathrm{bw} + 2\delta\gamma$, where $\delta\gamma$ is defined in §3.2. This would lead to an equation similar to equation (12) with the $\delta\gamma$ parameter occurring in the integrants and in the integrals' limits. The integration over ζ_e^2 could still be performed, but the next step, namely an integral over $\delta\gamma$ that takes into account the $\delta\gamma$ distribution [equation (5a)], cannot be performed analytically. Nevertheless, very good approximations can be obtained by employing equations previously established in this paper.

Indeed, if the electron beam angular divergence plays a dominant role with respect to the energy spread in the calculation of the X-ray flux within some acceptance cuts, a good approximation of $R_{\alpha,\mathrm{bw}}(\sigma_e, \sigma'_e)$ is obtained by using equation (13) and assuming $\theta_{\mathrm{bw}} = (\mathrm{bw}_{\mathrm{eff}})^{1/2}/\gamma_0$, where $\mathrm{bw}_{\mathrm{eff}}$ is the quadratic sum of bw and the standard deviation of μ_γ: $\mathrm{bw}_{\mathrm{eff}} = [\mathrm{bw}^2 + (2\sigma_e)^2]^{1/2}$. On the contrary, when the electron
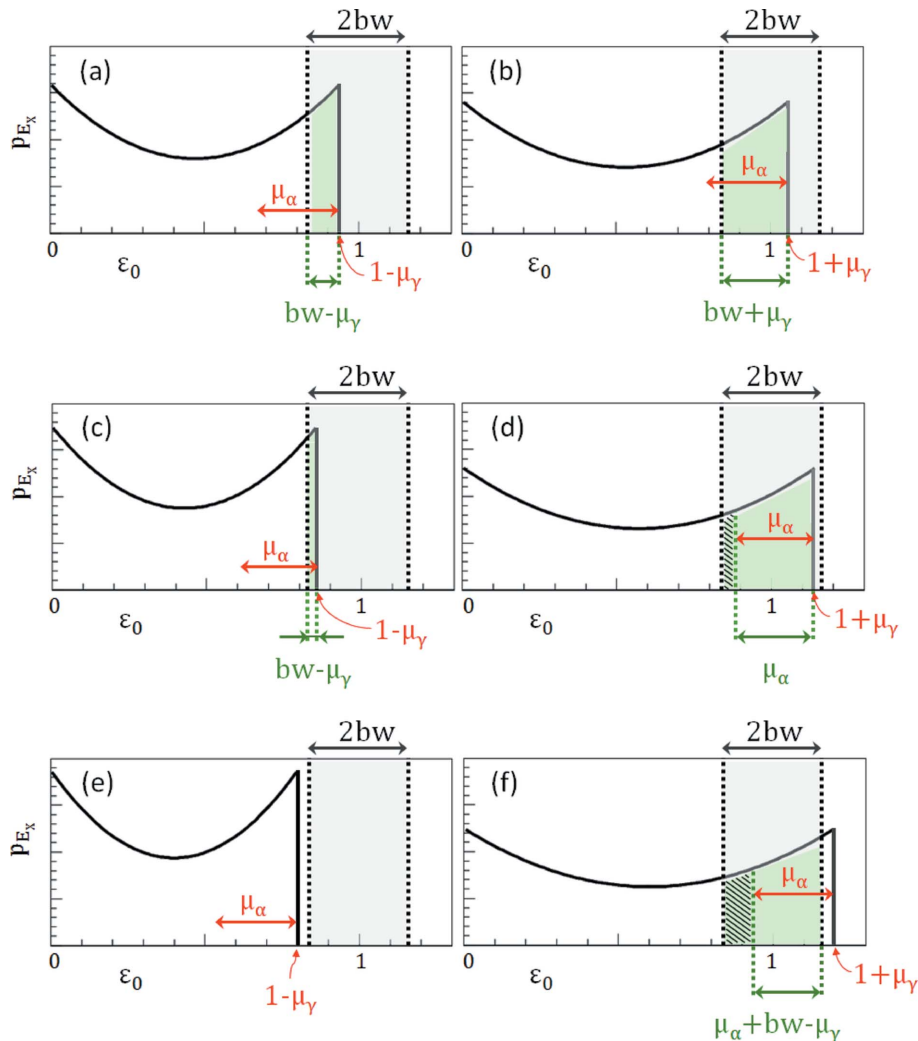
Figure 11
X-ray energy spectrum. The fraction of this spectrum which falls within the energy acceptance band is shown in green. The hatched bands represent X-rays which are eliminated because of the angular cutoff. Left panels correspond to $\delta\gamma$ negative, right ones to $\delta\gamma$ positive. (a) and (b) illustrate the cases where $0 < \mu_\gamma < \mu_\alpha - $ bw, (c) and (d) where $\mu_\alpha - $ bw $< \mu_\gamma < $ bw, and (e) and (f) where bw $< \mu_\gamma < $ bw $+ \mu_\alpha$.

beam energy spread is dominant with respect to the angular divergence, equation (15) must be used wherein the quantity $\sqrt{2\sigma_e}$ is replaced by the quadratic sum of $\sqrt{2\gamma_0^2\sigma_e'^2}$ and $\sqrt{2\sigma_e}$, resulting in the substitution $2\sigma_e \rightarrow 2\sigma_e + 2\gamma_0^2\sigma_e'^2$.

CAIN simulations and results of the modified equations (13) or (15) are shown in Fig. 13 for several values of α and bw. The discontinuities seen in the lines mark the use of equations (15) or (13) with the appropriate adaptation described above. When $2\gamma_0^2\sigma_e'^2 + $ bw $< [(2\sigma_e)^2 + $ bw$^2]^{1/2}$, equation (15) is used wherein $2\sigma_e$ is replaced by $2\sigma_e + 2\gamma_0^2\sigma_e'^2$. Otherwise, equation (13) is used where bw is replaced by $[$bw$^2 + (2\sigma_e)^2]^{1/2}$.

5. Additional comments and conclusion

We have derived analytic expressions for the total, the spectral and the angular X-ray fluxes of a Compton source according to the Compton kinematics and to the characteristics of the incoming electron and laser beams. The two dominant parameters governing the quality of such a source are the electron

beam energy spread and its divergence. We point out a limitation of the analytic calculation of the flux $R_{\alpha,\mathrm{bw}}$ in a given energy bandwidth *and* a specified solid angle when both the energy spread *and* the divergence of the electron beam must be taken into account in the calculation. Nevertheless, the expressions of $R_{\alpha,\mathrm{bw}}$ obtained when *either* the energy spread *or* the angular divergence of the electron beam is taken into account can still be used with an appropriate modification.

Analytic expressions (11), (13) and (15) provide the photon yield R_α within a given angular acceptance [equation (11)] and the photon yield $R_{\alpha,\mathrm{bw}}$ within both a given angular acceptance *and* a given energy bandwidth [equations (13) or (15)]. Table 2 summarizes the validity domains of these equations in terms of the selected Compton kinematic region and according to the energy spread and the angular divergence of the two incoming beams as long as they are within the parameters ranges of current electron and laser beams (see Table 1).

Within the large spectrum of X-ray applications in biomedical, cultural heritage or material science, specific X-ray

Table 2
Validity of equations (11), (13) and (15) in terms of the parameters.

The typical maximum values for current electron and laser beams shown in Table 1 are recalled. Each value indicates the upper limit of the parameter for which the equation is valid.

Parameters	$\gamma\alpha$ (rad)	bw	$\gamma\sigma_e'$ (rad)	$\sin\theta_c\,\sigma_L'$ (mrad)	σ_e	σ_L
e^- and typical laser values			0.25	10	A few %	A few ‰
Equation (11)	0.4		0.18	10	A few %	A few ‰
Equations (13) and (15)	Any	0.35	0.25	1†	2–3%	A few ‰

† For the particular cases where $\sin\theta_c\,\sigma_L' \simeq 1$–10 mrad, $R_{\alpha,\mathrm{bw}}$ is valid but is overestimated by $\sim$0.5–5% *via* the term R_{bw} (see §3.2).

beams are required depending on the analysis technique and the sample to be used. For instance, a narrow energy band-width is required in most of the X-ray diffraction experiments (Dik *et al.*, 2008) whereas therapy techniques such as stereo-tactic radiation therapy (Jacquet & Suortti, 2015) can relax the constraint on the spectral width. Thus, for an incoming electron beam with a given emittance, it may be beneficial to minimize its transverse size even at the expense of its divergence. This could be the case for instance in experiments where a large X-ray number is the main requirement, or when an as small as possible source size is needed to carry out some analysis technique (such as phase-contrast imaging techniques). On the other hand, the electron beam divergence may be minimized at the expense of the transverse size when a quasi-monochromatic X-ray beam is required.

Analytic formulas (11), (13) and (15) allow one to compute easily the spectral and spatial properties of an X-ray source based on photon backscattering, and highlight the beam parameters that play a key role for a given application. They should help when studying the feasibility of a particular experiment envisaged at some X-ray source.
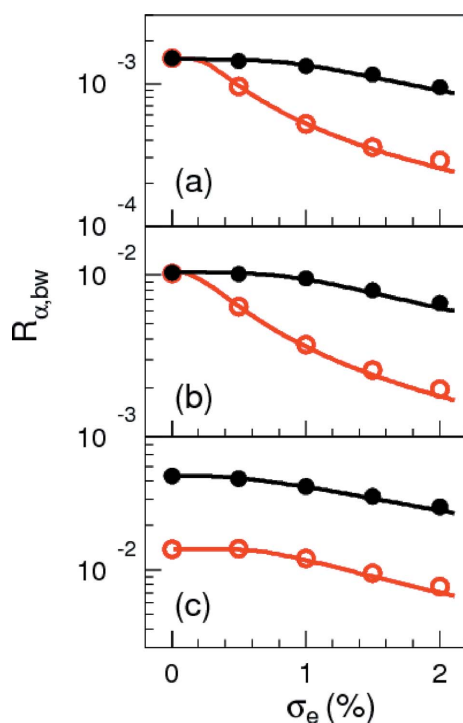
Figure 12
The ratio $R_{\alpha,\mathrm{bw}} = F_{\alpha,\mathrm{bw}}/F_0$ *versus* σ_e, for $\alpha = 1$ mrad (open circles) and 2 mrad (black bullets), and for (*a*) bw = 0.1%, (*b*) bw = 0.7% and (*c*) bw = 3%. $\sigma_e' = 0$ is assumed here. Lines are obtained by using the analytic expression (15) while points are *CAIN* simulations (the error bars are too small to be visible).
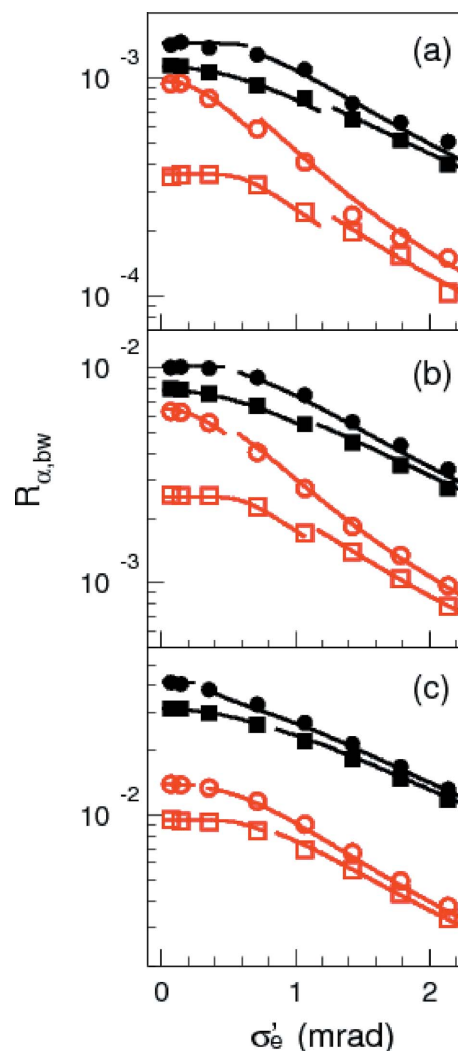
Figure 13
The ratio $R_{\alpha,\mathrm{bw}} = F_{\alpha,\mathrm{bw}}/F_0$ as a function of σ_e', for an electron energy spread σ_e of 0.5% (circles) and 1.5% (squares) and for a selection angle α of 1 mrad (open symbols) and 2 mrad (full symbols). (*a*) bw = 0.1%. (*b*) bw = 0.7%. (*c*) bw = 3%. Lines are the analytic calculations (see text), points are *CAIN* simulations (the error bars are too small to be visible).

Acknowledgements

References

Arnold, A. & Teichert, J. (2011). *Phys. Rev. ST Accel. Beams* **14**, 024801.

Dik, J., Janssens, K., Van Der Snickt, G., van der Loeff, L., Rickers, K. & Cotte, M. (2008). *Anal. Chem.* **80**, 6436–6442.

Donnelly, T. D. & Grossman, C. (1998). *Am. J. Phys.* **66**, 677.

Jacquet, M. (2014). *Nucl. Instrum. Methods Phys. Res. B*, **331**, 1–5.

Jacquet, M. & Suortti, P. (2015). *Phys. Med.* **31**, 596–600.

Rao, T. & Dowell, D. H. (2013). *An Engineering Guide to Photoinjectors*, http://arxiv.org/ftp/arxiv/papers/1403/1403.7539.pdf.

Schmüser, P., Dohlus, M. & Rossbach, J. (2008). *Ultraviolet and Soft X-ray Free-Electron Lasers.* Berlin: Springer.

Suzuki, T. (1976). KEK Technical Report 76–3, July 1976. KEK, Tsukuba, Japan.

Telnov, V. (2000). *Nucl. Instrum. Methods Phys. Res. A*, **455**, 80–89.

Variola, A., Haissinskii, J., Loulergue, A. & Zomer, F. (2014). *ThomX Technical Design Report.* LAL/RT 14–21. SOLEIL/SOU-RA-3629.

Yokoya, K. (2003). *User's Manual of CAIN*, http://lcdev.kek.jp/~yokoya/CAIN/cain235/CainMan235.pdf.